Trajectory Measurements on the Colorado Dust Accelerator Using a Dual Dust Coordinate Sensor

by

William R. Goode

Thesis defense date

April 3rd, 2018

Thesis advisor: Prof. Tobin Munsat

Department of Physics

Honors Council representative: Prof. Paul Beale

Department of Physics

Third reader: Prof. Zoltan Sternovsky

Department of Aerospace Engineering

Goode, William R.

Trajectory Measurements on the Colorado Dust Accelerator Using a Dual Dust Coordinate Sensor

Thesis directed by Prof. Tobin Munsat

The Dust Coordinate Sensor (DCS) is a dual detector instrument located on the beamline of the 3 MV hypervelocity dust accelerator at the University of Colorado Institute for Modeling Plasma, Atmospheres and Cosmic Dust (IMPACT). This instrument non-destructively measures the three-dimensional trajectories of charged, hypervelocity (3-8 km/s), micron-sized dust particles in flight by utilizing the image charge induced on grids of wire electrodes. Where previous peak detection was typically limited to dust particles carrying charges $> \sim 100$ fC, new signal processing techniques developed for DCS allow for effective trajectory measurements on particles carrying charges as small as 6 fC. The new signal processing also reduces false signal detections by $>$ 90%. The position measurements are matched by timestamp to the charge and velocity for each launched dust particle. Verification of the system was performed with independent impact location measurements on a target placed in the beamline. These measurements agree to within 1 mm^2 of the predicted locations using DCS trajectories. This study demonstrates the capability of the instrument including new processing methods. Precise trajectory measurement along the beamline enables new options for instrument calibration, scientific experiments, and improvement of the accelerator performance.

Dedication

To Mom (1963 - 2017). Thank you for all you have taught me.

Acknowledgements

I would like to thank Professor Tobin Munsat for supporting my growth as a researcher. By entrusting this project to me, he has given me the opportunity to discover an exciting new potential in myself. I would also like to thank Dr. David James for his mentorship during this project. My colleagues at the Institute for Modeling Plasma, Atmospheres, and Cosmic Dust have formed a community to which I am proud to belong. I would especially like to thank my wife, Kamrin. Her steadfast support, patience, and belief in me has been a source of strength throughout this exciting journey. I could not do this without her. This research was made possible by funding from the Center for Integrated Plasma Studies, the National Aeronautics and Space Administration, and the Solar System Exploration Research Virtual Institute.

Contents

Chapter

Figures

Figure

Chapter 1

Introduction

1.1   Cosmic Dust Research

Humankind has worked for centuries to understand the nature of the interplanetary and interstellar medium. For the environment near Earth and throughout the Solar System, a key feature is ubiquitous dust. An early sign of the dust permeating nearby space has been the Zodiacal Light seen in the early dawn and late dust sky (FIG 1.1). Though documented throughout the ages, it wasn't until around 1683 that the astronomer Giovanni Cassini made the first scientific investigations into the nature of the Zodiacal Light [2]. His disciple, Niccolo Fatio de Duilliers correctly hypothesized that this phenomenon is caused by Sunlight scattering off of tiny dust grains distributed throughout the ecliptic plane [2].

At the dawn of the space age, interplanetary dust research was motivated by both scientific curiosity, regarding history and dynamics, as well as engineering concerns, namely the hazard posed to space flight equipment and astronauts. New rocket technology enabled not only remote sensing observations from space but also the first in-situ measurements of cosmic dust. The first of such in-situ measurements were acoustical in nature using V-2 rockets in 1950 [2]. Though later shown to be inaccurately high by later dust instruments, the initial reported value of interplanetary dust flux near Earth marked an increased level of interest in the pursuit of cosmic dust research.

Interplanetary dust measurements offer a way of understanding the history and dynamics of the Solar System. This dust has diameters mostly on the micron or sub-micron scale and speeds of several km/s or higher. An impactor is said to travel at hypervelocity when its velocity exceeds the

Figure 1.1: Zodiacal light as seen at the European Southern Observatory [1]

speed of sound in the medium of the impact target [2]. During the early 1960s, initial studies into the nature of impact ionization of micron-sized dust particles traveling at hypervelocities began within the realm of interplanetary dust research [3]. Impact ionization occurs when the impactor strikes a target with sufficient energy to ionize both target and impactor material creating a cloud of neutral ejecta, ions, and electrons in the vicinity of the impact crater [2]. Using a static electric field, the ions can be separated so that the constituents of the impactor can be measured. Space-borne dust instruments aboard Pioneer 8 and 9 were the first to use impact ionization to make in-situ measurements of cosmic dust [2, 4]. Later dust instruments used time-of-flight (TOF) mass spectroscopy to measure the chemical composition of impacting dust particles. The Helios space probe was the first to carry dust instruments using this method to measure the chemical composition of interplanetary dust during the 1970s [2, 5]. More recent dust instruments for which impact ionization is a key feature of measurement design include the Lunar Dust Experiment (LADEX) flown aboard the Lunar Atmosphere and Dust Environment Explorer (LADEE) mission and the Cosmic Dust Analyzer (CDA) flown aboard the Cassini mission [6, 7].

Cratering done by cosmic dust particles is another interesting phenomenon that is investigated in this field of research. Developing and using models that relate the characteristics of the impactor and crater enables us to utilize observed cratering effects to infer information on the cosmic dust that causes it. SDC relies on such cratering effects in order to measure low dust fluxes as the New Horizons spacecraft traverses the Solar System [8, 9].

Cratering by cosmic dust plays a significant role in space weathering. The Long Duration Exposure Facility (LDEF) remained in low earth orbit for nearly six years in order to study the effect of space weathering on various surfaces and materials. After being retrieved from orbit, thousands of impact-related features were characterized and documented [10]. Studies on the micron and sub-micron diameter craters found on lunar samples conducted during the 1970s have helped quantify the historical dust flux in our region of the Solar System [2]. Such studies form an empirical basis for developing cratering scaling models. For example, by using the observed characteristics of a crater to infer the density of the impactor, it is possible to determine the source of the dust flux as
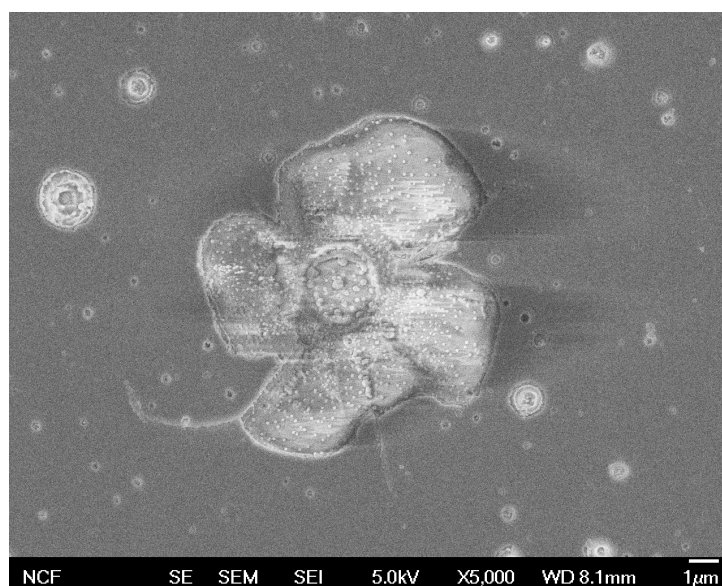
Figure 1.2: Image of cratering caused by iron dust particles on a glass surface taken with the field emission scanning electron microscope (FESEM) at the Nanomaterials Characterization Facility at the University of Colorado, Boulder. This image shows a large impact crater approximately 2 μm in diameter surrounded by several smaller craters. The process creating the large crater also shattered some of the surface resulting in a flower-like pattern.

either asteroidal or cometary [2]. An example of craters created in the laboratory are shown in FIG 1.2. By replicating the measured effects of dusty plasmas and impacts occurring in space we can better understand the environment in which such measurements are taken. This has historically been a motivation behind the development of laboratory simulations of cosmic dust.
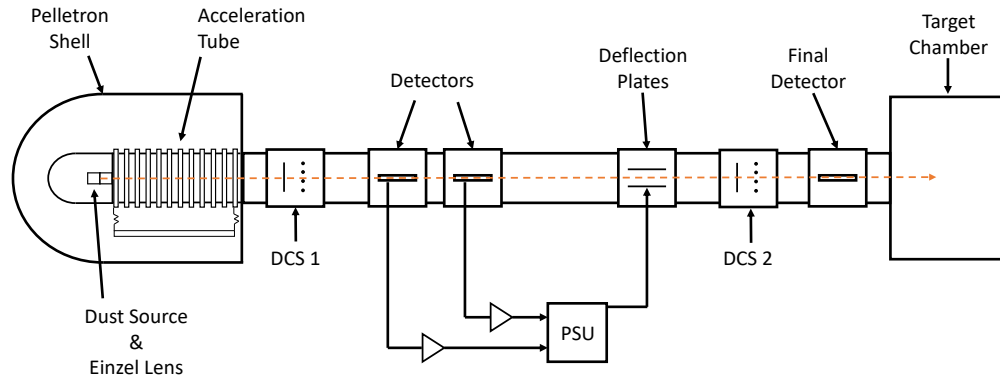
Figure 1.3: Schematic of the University of Colorado dust accelerator. The particles contained in the dust source are charged before entering the acceleration tube. The Einzel lens pre-focuses the particle beam using a shaped static electric field. The first two detectors measure the particle charge and velocity, which the PSU utilizes for downselection. The deflection plates are grounded by a pulse from the PSU, allowing individual particles to continue towards the target chamber. The final detector verifies the down-selection by the PSU and deflection plates. The Dust Coordinate Sensor (DCS) measures particle trajectory using two in-beam detectors, DCS 1 and 2.

1.2   Electrostatic Dust Accelerators

Electrostatic dust accelerators with the capability to launch micron and sub-micron diameter charged dust particles were first built in the early 1960s. One was built by Space Technology Laboratories in Redondo Beach, California while the other was built by the Max Planck Institute in Heidelberg, Germany. It was these two laborites that made the first direct measurements of impact ionization and obtained the first TOF mass spectra from dust particle impacts [11, 3, 12, 2].

Instrument calibration is used to establish the correlation between signal and dust particle characteristics, which is essential for in-situ measurements in space. Laboratory experiments related to the study of dust impacts are currently performed using the 3 MV hypervelocity dust accelerator at the Institute for Modeling Plasma, Atmospheres and Cosmic Dust (IMPACT) at the University

of Colorado, Boulder [13]. Shown in FIG. 1.3, this accelerator utilizes a static electric potential generated by a Pelletron chain induction system [14]. The dust particles are charged in a ~ 1 cm^3 volume reservoir by a needle at an adjustable potential of 1-20 kV. Once charged, each particle is accelerated down the beamline through a series of three image charge detectors before reaching the target chamber. Particle velocity is measured using time-of-flight between the first two detectors [13]. Particles reach velocities ranging from approximately 0.5 to 100 km/s with diameters ranging from tens of nm to ~ 5 μm.

Since the size of individual particles from a given dust source are typically inhomogeneous, the characteristics (charge,velocity, etc.) of each accelerated particle cannot be predetermined [13]. Therefore the particle beam itself consists of random discrete dust events. The Particle Selection Unit (PSU) down-selects in order to provide the experimenter control over the parameters of particles reaching the target [13]. The PSU utilizes deflection plates, otherwise known as the gate, that generate a static transverse electric field diverting particles out of the beamline as a default state. The gate is opened at the precise time in order to allow a desired particle to pass through to the final detector and target chamber. This is enabled by a field programmable gate array (FPGA) that performs fast real-time calculations based on signals generated by the image charge detectors.

1.3   Dust Particle Trajectory Sensors

Dust particle trajectory sensors using non-destructve techniques were first developed for the purpose of supplementing space-borne dust instruments [15]. Earlier methods of measuring particle trajectories used thin films that were penetrated by incoming dust particles. This destructive technique had particular disadvantages since this would alter the particles' angle of incidence, introduce error in the TOF mass spectra measurements due to film fragments, and limit the minimum mass and velocity of measurable particles since they required sufficient kinetic energy to penetrate the film. Non-destructive techniques, such at the method of charge division, leaves the particle's trajectory undisturbed, maintaining the integrity of composition measurements while increasing

the precision of trajectory measurements. Knowing a measured dust particle's trajectory helps in determining its origin, leading to spatial compositional mapping of an environment [15]. In addition to aiding the calibration of space-borne instruments in the laboratory, measuring dust particle trajectories is an important capability for dust accelerator beam diagnostics.

Particle position measurements on the beamline must be made by a dedicated set of detectors. This has been done in the past on a similar particle accelerator by a position detector at the Max Planck Institute in Heidelberg, Germany [16]. This detector uses charge induced by a particle on four pairs of parallel plates. The system was calibrated to use the amplitude ratios to compute particle position at a single location on the beamline. However, in order to obtain a particle's trajectory, and thereby its position anywhere along the beamline, position measurements must be made at more than one location.

The Dust Coordinate Sensor (DCS) was developed for the purpose of providing particle position information along the beamline, which has been unknown until recently. This instrument consists of two detectors installed 4 m apart on the beamline. Each detector measures two-dimensional position in the plane orthogonal to the beamline. This new instrument is capable of measuring three-dimensional trajectories of each dust particle in flight. This added capability allows us to profile the particle beam as well as locate individual particle impact locations with high precision.

This new capability promises to play a crucial role in improving the efficiency of the dust accelerator. For example, we will be able to profile the dust beam's width and focal point and empirically determine its response to adjustments to focusing controls. Steering the beam can be done using live feedback on the dust beam position rather than throughput, which was previously the only technique available. This thesis describes the measurement methods, signal analysis, and the most recent performance tests of DCS. The goal is to improve the dust accelerator's ability to support cosmic dust and dusty plasma research using more precise measurements, richer data, and with higher throughput.

Chapter 2

DCS Concept and Operation

2.1   Method of Measurment

DCS is an in-beam instrument that uses charge induction on a series of eight 0.48 mm thick wire electrodes to measure particle position. The wire electrodes are placed within a 2.5 × 2.5 cm square channel mounted on a removable 6 inch flange on the beamline. The wire electrodes are arranged into two separate planes of four wires orthogonal to the direction of the beamline. The first wire plane consists of four vertical wires while the second plane consists of four horizontal wires all spaced by 5 mm. The wire planes themselves are separated by 5.1 cm from each other in the z-direction. Together they form 25 regions through which a particle might fly. Each DCS detector has an open area of ∼80%. A detailed description of the mechanical design of the individual DCS detectors is presented in Northway *et al.* [17]. A schematic of the detector design is shown in FIG 2.1. Throughout this thesis, we later refer to a set of four vertical or horizontal wires as a "wire plane", each DCS detector consisting of two wire planes simply as a "detector", and the system consisting of both detectors as the "instrument".

As each particle travels through the wire planes, it induces image charges on the wire electrodes. The greatest induced charge occurs on the nearest wires, and the ratio of peak induced charge between the two nearest wires is a unique function of particle position. This method of charge-dividing was first applied by Auer *et al* to measure the trajectories of charged cosmic dust particles [15]. The vertical wire plane is used to determine the horizontal (x) position while the horizontal wire plane is used for the vertical (y) position. Each wire electrode is connected to a
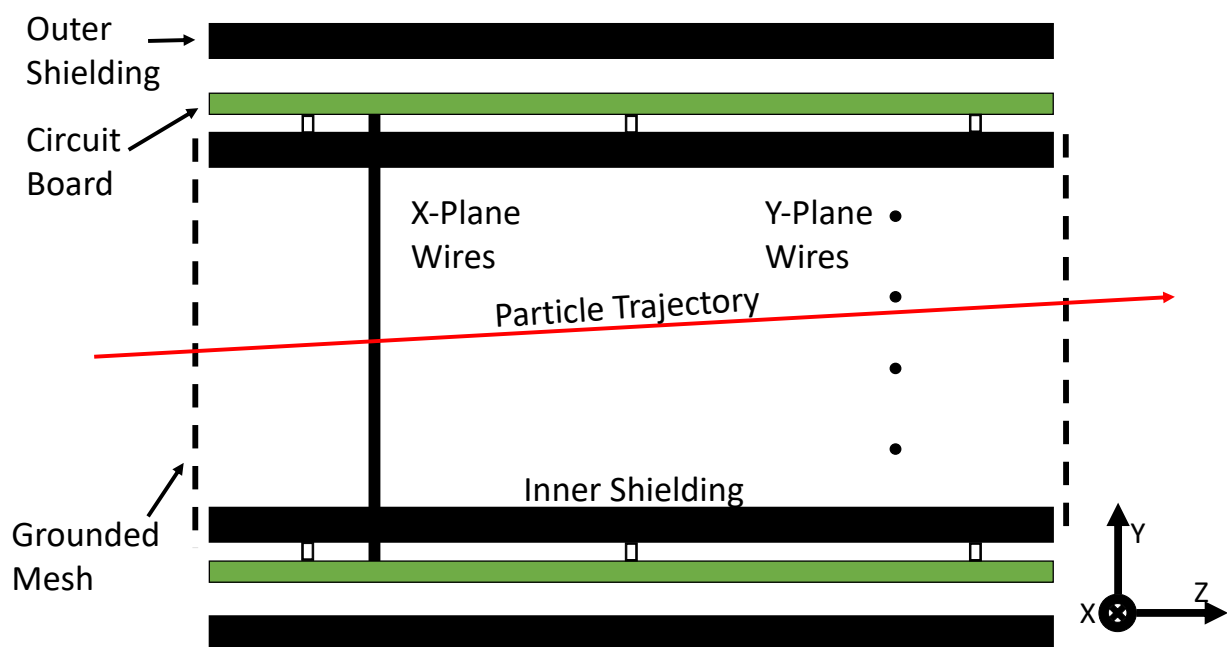
Figure 2.1: Cutaway schematic diagram of a single DCS detector. Wire electrodes in the first wire plane run vertically and measure x-position while the wires in the second plane run horizontally and measure y-position. The wire planes are separated by 5.1 cm along the beam direction.

separate charge sensitive amplifier (CSA) so that the induced charge on each wire electrode can be measured. This concept is illustrated in FIG. 2.2.

Note: The accelerator uses a right-handed coordinate system with the z-axis pointing along the dust particle beam direction, the y-axis pointing up from the facility floor, and the x-axis pointing to the left when looking in the positive z-direction. Throughout this thesis, however, plots showing particle locations adopt the convention where the x-axis points in the opposite direction to this. This is because impact locations on targets exposed to the beam will be aligned in the orientation where the positive z-direction points into the impact surface. Plots of projected particle locations will therefore be shown with the positive x-direction pointing to the right.

Voltage waveforms are acquired in order to determine the induced charge on each wire as the particle traverses the wire plane. Given the complex geometry of the instrument (due to the finite length of the wires and the multi-layered shielding), the relation between the eight induced charges and particle position has been computed from first principles using finite-element simulations performed using COULOMB software [17]. This provides a series of lookup tables for the relative induced charge values for each xy-position over the cross-sectional area of the instrument (12×12 mm) using a 0.5 mm step size. These lookup tables are used by an interpolation software routine in order to determine the best match between arrays of measured peak voltages and corresponding xy-positions at the location of each DCS detector.

2.2   Instrument Operation

2.2.1   Set Up

Each DCS detector (DCS 1 and 2) captures transient waveforms utilizing CSAs from each of their eight wire electrodes. The detector sends 8 CSA outputs via a DB 25 feedthrough carrying the signals from each wire electrode. The analogue signals are digitized by Joerger Model TR "CAMAC" multi-channel analogue digitizers, otherwise referred to as the data acquisition cards (DAQs). The DAQs provide 12 bit resolution and are configured to acquire data at a rate of 40
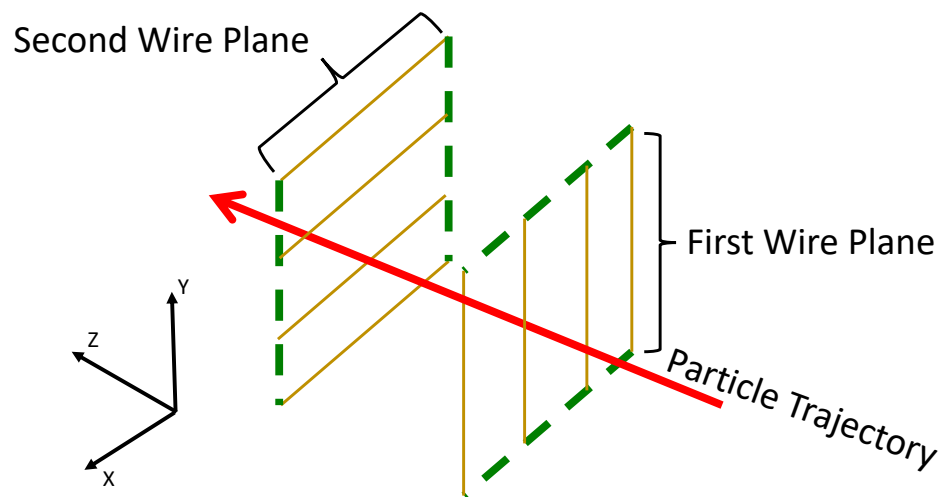
Figure 2.2: The Dust Coordinate Sensor operational concept. The particle flies through a plane of four vertical wires (measuring x-position) then a plane of horizontal wires (measuring y-position). Each wire electrode is connected to CSA, which provides voltage waveforms.

MHz. Each DCS detector utilizes 8 of the 16 analogue input channels on their respective DAQ. The DAQs are operated using a CAMAC crate and are controlled by a LeCroy 8901A GPIB control interface. The 8901A is paired with a library of LabView functions, which are incorporated in a single software program for DCS data acquisition.

In order to capture the signal from a passing particle, the system is triggered externally by a single source corresponding to a dust event. The number of samples for pre-trigger on DCS 1 as well as the post-trigger on DCS 2 is sized based on the data acquisition sampling rate, spacing of DCS 1 and 2 in relation to the PSU, and the minimum expected particle velocity using the equations

$$PreTrigger = S\left(\frac{D_1}{v_{min}}\right) \tag{2.1a}$$

$$PostTrigger = S\left(\frac{D_2}{v_{min}}\right) \tag{2.1b}$$

where S is the sampling rate (samples/second), D_1 is the distance from DCS 1 to the PSU (m) along the beamline, D_2 is the distance from the PSU to DCS 2 (m), and v_{min} is the minimum expected velocity (m/s).

2.2.2   Data Acquisition

Each DAQ is triggered externally by the accelerator's FPGA. The FPGA tracks data acquired by the accelerator's two separate image charge detectors [13]. The data from these detectors provide velocity (using time of flight) and total charge of individual particles. Once a particle is detected, the FPGA sends a TTL pulse to the PSU allowing the particle to enter the target chamber. This pulse is also sent to the DCS DAQs in order to trigger at the appropriate time. The transient waveforms from DCS are matched by timestamp with corresponding waveforms from the image charge detectors for each particle so that each DCS dataset is matched to that particle's metadata set from the accelerator. An illustration of the data acquisition, control, and analysis scheme is shown in FIG. 2.3.

Since the particle's charge and velocity are not known ahead of time, care must be taken to
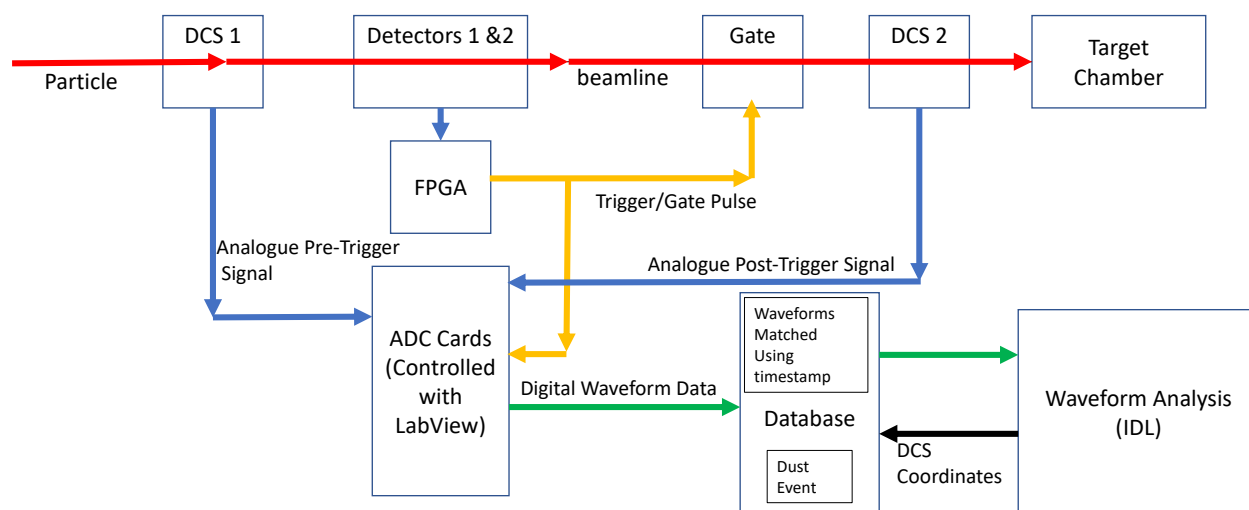
Figure 2.3: Data acquisition, control, and analysis scheme. DCS 1 continuously records transient data. After the particle passes through detectors 1 and 2, the FPGA performs a fast real time calculation. If the particle matches pre-selected parameters, a TTL gate pulse is sent to allow the particle to continue onto the target chamber. This same pulse is used to trigger both DCS DAQs. The transient data containing the original waveforms is then uploaded, digitized, and stored in the database. The waveforms are later retrieved for analysis. Finally, the calculated coordinates are stored back in the database with the dust event.

distinguish signal peaks from random noise spikes. To save space, we preprocess the waveforms before saving them to the database. This provides DCS the ability to run reliably in parallel with any experiment on the accelerator without overburdening the database or post processing operations.

The first stage of preprocessing the waveform involves separating each channel into separate arrays and running them through a median filter. This helps by smoothing out the waveform in order to detect a possible signal. Since each raw waveform is much longer than any expected signal, the first 10% of the waveform (a "signal-free" section) is used to compute the standard deviation of the background noise. It was empirically determined that a waveform containing a dust particle signal should have an amplitude at or above 6 times the standard deviation of the noise. Though there are undoubtedly dust particle signals with lower signal to noise ratios, the nature of the noise on the DCS channels makes detecting these particles prohibitive at this time.

The first and second sets of four channels are separated in the data acquisition program to correspond with the first and second wire planes respectively. The time index of the detected signal on the first wire plane should naturally precede that of the signal detected on the second wire plane. This fact is used as a consistency check in the final stage of preprocessing the waveforms. Adding these steps to peak detection reduces false signal detection by more than 90 %. Once this process is complete, the unfiltered waveforms are trimmed in order to contain the complete signal while optimizing database space usage.

2.2.3   Signal Processing

Using code written in Interactive Data Language (IDL), the set of 16 waveforms, corresponding to the eight channels of each DCS detector, is retrieved from the database for analysis. The set of eight waveforms from each detector are separated into two sets of four, corresponding to each wire plane (FIG 2.4). The values on the COULOMB-calculated lookup tables have been calculated for particles within a wire plane, which is also the point of maximum induced charge on the nearest wire. It is important to note that the peak voltage does not occur on all four channels while the

particle is in the wire plane. Due to a shielding effect, wires on the opposite side of the nearest wire actually exhibit a dip in amplitude while the particle is within the wire plane [18]. For this reason, we utilize the highest peak value of the four channels of the wire plane to determine the wire-plane crossing time and use the corresponding time index to acquire the coincident signals from all four channels. The waveform values corresponding to this time index are taken as the signal values to be analyzed.

Since smaller particles carry less charge, detecting them using induced charge on wire electrodes is relatively difficult. This is because signals from particles carrying less than a few fC of charge are hidden in the background noise. The noise characteristics on the channels makes peak detection unreliable for a low SNR. In order to decrease the size of the smallest detectable particle by DCS, a new technique for finding low SNR signals was developed.
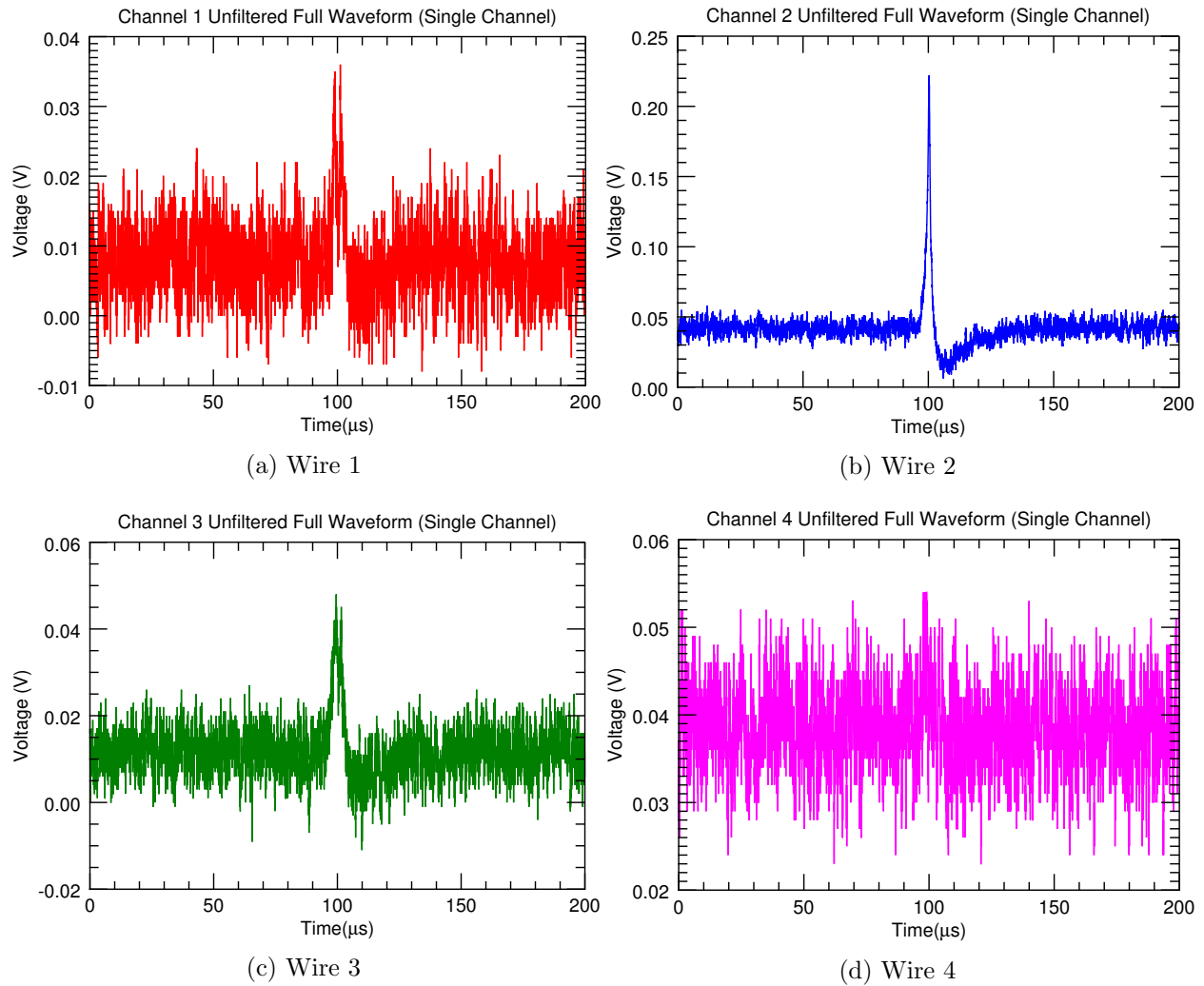
Figure 2.4: Unfiltered voltage waveforms from the first four wires of DCS 1 representing the first (vertical) wire plane. In this example, the 28 fC particle passed between wires 2 and 3 approximately 0.6 mm from wire 2.

The first step of this technique is to smooth the waveforms using boxcar averaging with a wide window size. This "coarse" smoothing is only meant to generally locate the signal within the waveform (see FIG. 2.5). The original peak values are distorted by the course smoothing process and therefore cannot be used in the position analysis. The approximate time index of the signal is found by locating the max value on the coarsely smoothed waveform. A time window around this peak value is cut out of the original unfiltered waveform. This leaves us with a much smaller waveform containing the signal while reliably eliminating the surrounding noise spikes.

After subtracting the DC baseline, we use boxcar averaging with a window size that depends on particle velocity and DAQ sampling rate (see FIG. 2.6). The sampling rate is set by the DAQ hardware capabilities, which is kept constant at 40 million samples per second. Velocity is calculated using time of flight from the main detector waveforms and is fed to the DCS positioning software routine. Due to the sampling rate, the fidelity of the peak value is not maintained with any boxcar averaging for particles with velocities above 8 km/s. For slower particles, we use a dynamic window size, which ranges up to 10.6 time divisions of 25 ns for 1 km/s particles. The window size is calculated with the empirically derived expression

$$windowsize = 10.6 - 0.00131 * velocity \tag{2.2}$$

where window size is given in time divisions and velocity is in m/s. Once the time index for the highest peak value on the wire plane is found for the channel corresponding to the nearest wire, it is used to retrieve the coincident signal values on the other three channels in the wire plane.

Each set of four signal peak values for the wire planes are normalized and compared with the lookup tables using an interpolation routine. This returns the best matching xy-positions for DCS 1 and 2. Once the waveforms from both DCS and image charge detectors are processed, metadata of each particle's characteristics (e.g. mass and velocity) are paired with xy-positions for two locations along the beamline and stored in the database together.

2.3 Position Data Handling

Each DCS measurement is assigned a quality factor ranging from 0 to 5. This provides an estimate of the effectiveness of signal processing and the ability to select for a desired level of reliability in subsequent database searches. Quality is determined by signal-to-noise ratio (SNR) as well as by the relative induced charge between adjacent wires for a given plane. Signals with an SNR > 250 are considered to be high quality and are assigned a quality factor of 5. Those with an SNR < 20 are considered "very weak" and are assigned a quality factor of 0. Wire strikes are detected using the relative amount of charge induced on a particular wire. A normalized peak value > 0.99 indicates a wire strike and the position measurement is given a quality factor of 0.

Particle trajectory calculations assume straight-line trajectories for every particle. The vertical drop of each particle due to gravity is given by,

$$VerticalDrop = \frac{1}{2}g\left(\frac{z}{v}\right)^2 \tag{2.3}$$

where g is 9.8 m/s^2 , v is the particle velocity, and z is the total distance traveled down the beamline. For a particle with a velocity of 3 km/s , which is on the slow end of the expected velocity range based on accelerator performance, and a travel distance of approximately 6 m from dust source to target chamber, the vertical drop of the particle is approximately 20 μm. This is significantly less than the minimum error, discussed further in chapter 3, so it is ignored.

Using the xy-coordinates from both DCS 1 and 2, the transverse position of each particle can be projected anywhere along the beamline using the equations

$$x_{projected} = \left(\frac{x_2 - x_1}{d}\right)z_{projected} + x_1 \tag{2.4a}$$

$$y_{projected} = \left(\frac{y_2 - y_1}{d}\right)z_{projected} + y_1 \tag{2.4b}$$

where x_1 and y_1 are the coordinates measured by DCS 1, x_2 and y_2 are the coordinates measured by DCS 2, d is the distance from DCS 1 to DCS 2, and $x_{projected}$ and $y_{projected}$ are the coordinates for any point, $z_{projected}$, along the beamline.

DCS provides the capability to show live beam profile information to the accelerator operator. This is done using a live plot software program developed in LabView (FIG 2.7). By retrieving DCS position measurements from the database and performing calculations based on equations (2.4a) and (2.4b), the operator can select any point along the beamline (including inside the target chamber) and see transverse positions of each dust particle detected by DCS during an experiment. This capability provides real-time feedback of the dust beam profile based on adjustments made to beam control parameters such as xy-steering and Einzel lens voltage.

2.4   Conclusion

Using the FPGA for triggering allows DCS to utilize both detectors to measure position at two locations along the beamline. Signal processing techniques involving smoothing and peak detection allows the interpolation routine to find the best match from the position look-up table. Given the nature of the charge signals and the background noise on the instrument channels, detectability of a particle by DCS is limited based on size and velocity. The sensitivity of DCS is empirically determined and discussed in chapter 4. Once particle position measurements are made, we must determine the error. Measuring the error for each position measurement allows us to characterize the overall precision of DCS. This is the topic of the next chapter.

(a) Unfiltered

(b) Coarse Filtering
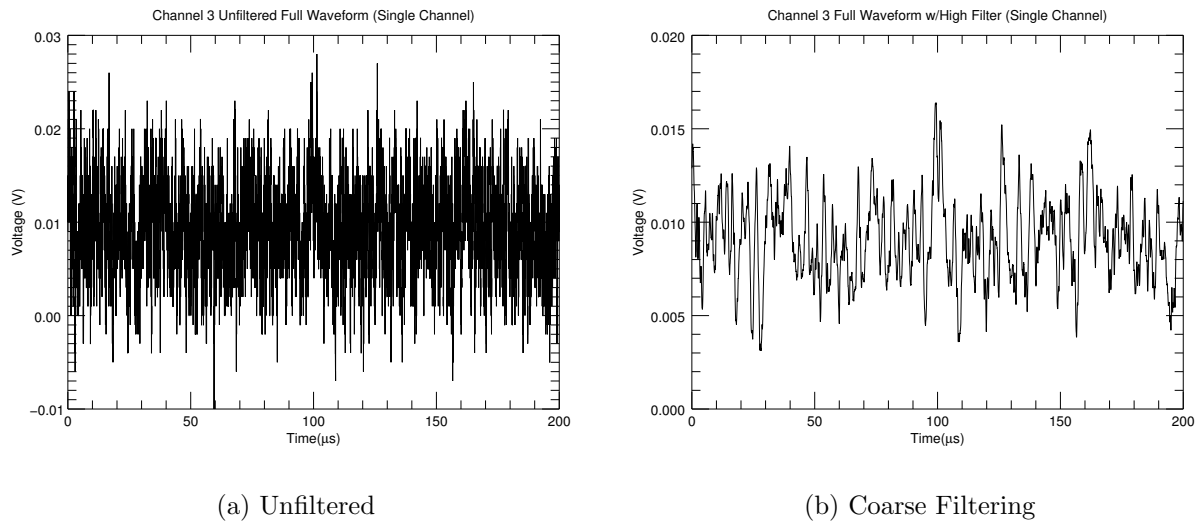
Figure 2.5: Example of a waveform with low SNR signal. In 2.5a simple peak detection will not work for finding the peak value of the signal, which can be seen in the middle of the waveform. This is due to random noise spikes with amplitudes exceeding that of the signal scattered throughout the waveform. Using boxcar averaging with a wide window size, the noised spikes are effectively cut down so that the signal is shown more clearly near the middle time index in 2.5b. By locating the time index corresponding to the max value, we can cut a narrower time window out of the original waveform in order to perform more precise smoothing.

(a) 2.8 km/s

(b) 4.9 km/s
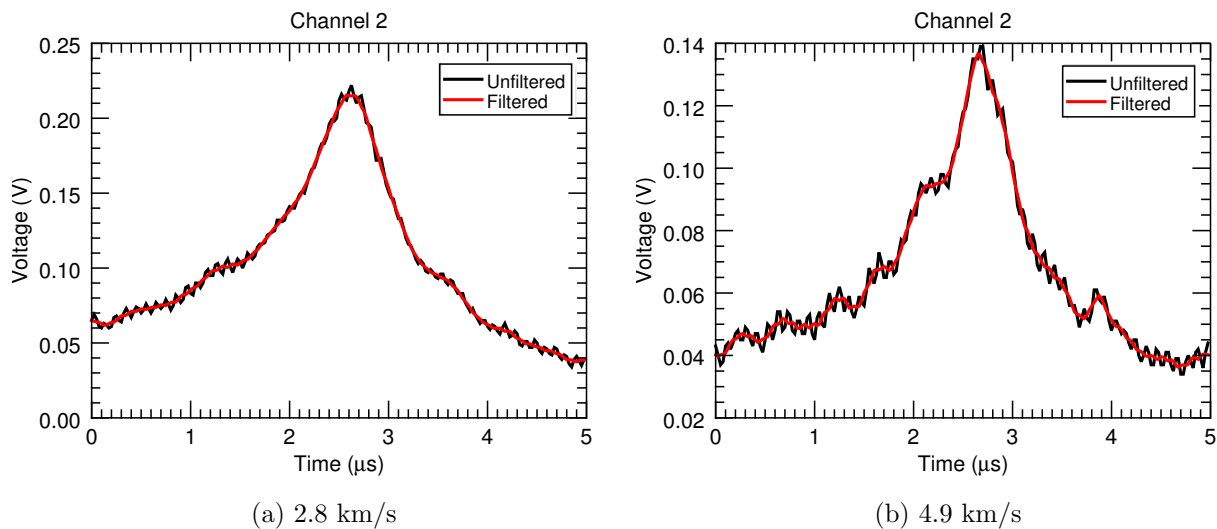
Figure 2.6: Two examples of optimal signal smoothing using boxcar averaging. Smoothing adjusts to the particle velocity. The smoothed waveform (red) bisects the peak-to-peak values of the noisy unfiltered waveform (black). The smoothed waveform provides the best approximation of the true peak value.
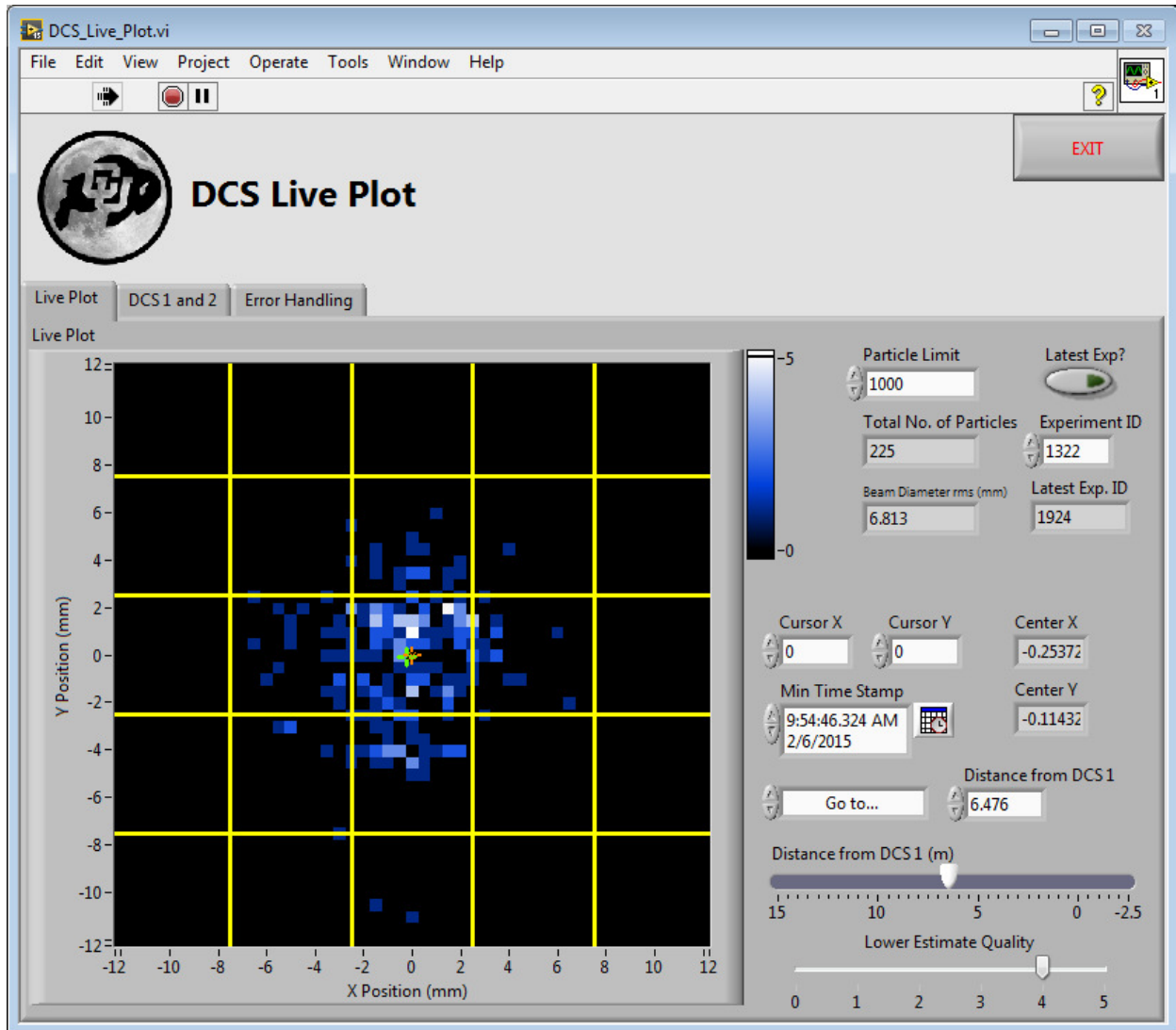
Figure 2.7: DCS Live Plotter retrieves coordinates kept in the database for each dust event and displays the projected position for any location along the beamline using an intensity plot (looking towards the target). This program also computes the Gaussian center of the beam (green cursor). This provides the accelerator operator real-time feedback on the beam profile. This particular image shows the distribution of dust particle positions at the center of the target chamber.

Chapter 3

Precision and Error

3.1   Introduction

The main objective of DCS for the accelerator is to significantly reduce the uncertainty in particle position from approximately 1 cm^2, which is based on the collimation of the beam by the pick-up tubes. Each position measurement made by DCS has an error introduced by the electronic signal itself due to the background noise on the CSAs. The signal quality varies based on the particle size and proximity to the wires. This implies that the error is partly determined by the position of the particle within the detector's cross-section. The positioning of each detector relative to beamline also contributes to error. Since each detector is not precisely aligned with beamline, each position measurement made by a detector has a systematic error. This chapter discusses how both electronic and systematic error are characterized so that two-dimensional position uncertainty can be computed for each dust particle position at any point along the beamline.

3.2   Electronic Error

Background noise in the electronic signals leads to random uncertainty in each position measurement made by DCS 1 or 2. Various factors arising from the electronic signal itself affect the error in the position measurement and are discussed below. Error for a position measurement is calculated for each dust event using the equation presented in Northway *et al*

$$\Delta r = \Delta R \left(\frac{dr}{dR} \right) \tag{3.1}$$

where Δr is the uncertainty in position for either x or y (i.e. Δx or Δy), R is the ratio of induced charge between the two nearest wires, and $\frac{dr}{dR}$ is the inverse of the spatial gradient of the voltage ratios determined from the simulation look-up tables (where r is either x or y) [17]. Therefore, the uncertainties, Δx and Δy, depend upon both the quality of the signal and measured position within the cross-sectional area of simulated ratios. The uncertainty of the charge ratio, ΔR, depends on the quality of the signals. Starting with the voltage waveform recorded during the dust event, ΔR is calculated using the following process.

The charge induced on the closest and second closest wire is given by

$$Q_{1,2} = \frac{V_{peak1,2}}{K} \tag{3.2}$$

where V_{peak} is the peak value from the voltage waveform for the corresponding channel, which is divided by the CSA sensitivity, K. Each channel CSA on DCS has been calibrated to approximately 1.215×10^{13} V/C [17] .

The voltage ratio of induced charge used to determine position within a wire plane is given by

$$R = \frac{Q_1}{Q_2} \tag{3.3}$$

where Q_1 is the highest induced charge and Q_2 is the second highest induced charge.

The charge noise, ΔQ, is computed using the voltage root mean square (rms) of the noise floor as well as the CSA sensitivity. The rms on each channel for both DCS 1 and 2 is approximately 5 mV. For a given channel, the charge-to-noise ratio $QNR = \frac{Q}{\Delta Q}$, where Q is the total charge of the particle measured by the main pick-up tube detectors. The formula for the ratio uncertainty is given by:

$$\Delta R = R\sqrt{\left(\frac{\Delta Q_1}{Q_1}\right)^2 + \left(\frac{\Delta Q_2}{Q_2}\right)^2} \tag{3.4}$$

This can be simplified to

$$\Delta R = \frac{R}{QNR}\sqrt{\left(\frac{1}{C_1}\right)^2 + \left(\frac{1}{C_2}\right)^2} \tag{3.5}$$

where $C_{1,2}$ is the fraction of the particle's total charge induced on the first and second wire respectively [17]. C_1 and C_2 are computed using the following empirically determined fuctions,

$$C_1(r) = e^{-|r|/0.7} + 0.1 \tag{3.6a}$$

$$C_2(r) = 0.043149|r| + 0.001 \tag{3.6b}$$

where $|r|$ is the absolute distance between the dust particle and the nearest wire in the plane in mm. Equations 3.6 were determined using an ensemble of paired wire voltage peak values and position measurements as shown in FIG 3.1.

At the location of each wire, however, the ratio, R, presents a mathematical singularity since as the absolute distance from a wire approaches zero, $|r| \to 0$, either Q_1 or $Q_2 \to 0$, implying $\frac{1}{C_{1,2}} \to \infty$, which leads to an uncertainty that does not make physical sense. Take, for example, a particle position (x or y) measured at the midpoint between two wires. Since the wires are 5 mm apart, $R \sim 1$ and the highest possible uncertainty is $\pm$ 2.5 mm. As measured position approaches one of the wires, uncertainty must decrease since the induced charge ratio will more clearly indicate position. When a particle's image charge is induced almost entirely on one wire within the wire plane, the uncertainty should converge to a small finite value rather than blow up to infinity. To ensure this happens during uncertainty calculations, we mitigate such singularities by first ensuring that the highest possible ratio is hard coded as an arbitrarily high value to avoid producing a divide by zero error. We additionally take twice the absolute distance from the wire ($|2r|$) to be the uncertainty whenever the induced charge ratio begins to approach a singularity. In other words, as the particle position approaches the wire, uncertainty should fall; therefore, if the uncertainty computation exceeds twice the distance from the nearest wire, where the ratio acts like a singularity, we can take $|2r|$ as being a better representation of uncertainty. The factor of 2 comes from the possibility that the dust particle may be on the opposite side of the wire from the measured position since the signal on the second nearest wire is so small. Such mitigations are only necessary for regions close to the wires ($|x| \sim < 0.1$ mm) whereas most position measurements within the wire plane will involve uncertainty calculations based on R.
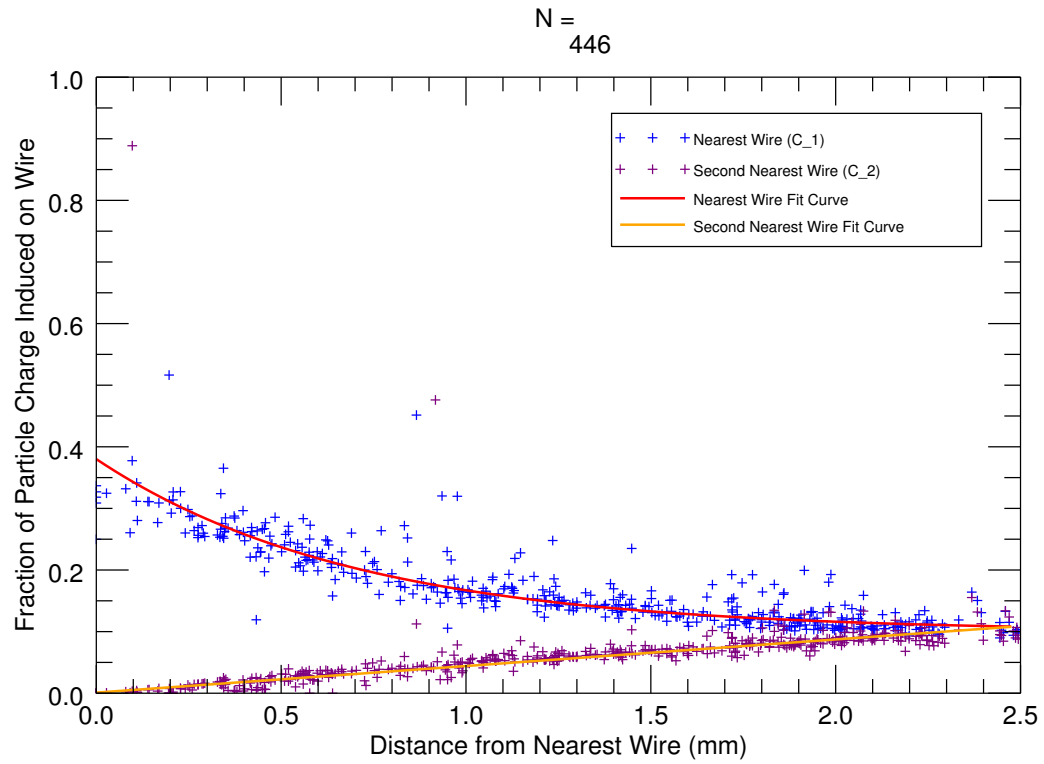
Figure 3.1: An ensemble of particle position measurements were used to determine the best fit function for computing the fraction of the dust particle's charge induced on the nearest wire, C_1 (red curve), as well as that on the second nearest wire, C_2 (orange curve). Both are functions of the dust particle's distance from the nearest wire.

The gradient, $\frac{dr}{dR}$, is found by interpolation using the look-up tables. This is done for each wire plane corresponding to either the x or y position measurement. With both R and $\frac{dr}{dR}$ computed for a particular DCS measurement, the uncertainties for both x and y are given as functions of measured position:

$$\Delta x_{electronic} = \Delta R_x \left(\frac{dx}{dR_x} \right)\Bigg|_{x=x_{measured}} \tag{3.7a}$$

$$\Delta y_{electronic} = \Delta R_y \left(\frac{dy}{dR_y} \right)\Bigg|_{y=y_{measured}} \tag{3.7b}$$

R_x and R_y are the wire ratios in the wire planes measuring x and y position respectively. The uncertainties, $\Delta x_{electronic}$ and $\Delta y_{electronic}$, are the minimum uncertainties for the xy-position relative to the center of the instrument. $\Delta x_{electronic}$ and $\Delta y_{electronic}$ for DCS 1 and 2 are computed for every dust event during post-event signal processing and stored in the database.

3.3   Systematic Error

The position of each DCS detector relative to beamline center introduces a source of systematic error. The precise positions of each DCS instrument relative to beamline (henceforth referred to as the offsets) are difficult to determine directly with high precision. This is due to the mechanical placement of the instrument in the beamline. An alternative method for determining the offsets for DCS 1 and 2 involves taking an ensemble of trajectory measurements that pass through multiple apertures (the three pick-up tube detectors in this case) to the target chamber and using the known mechanical placements of the appertures as a reference.

Aligning the main detector is done by visually centering the pickup tube with a high precision telescope aligned to the beamline. This is relatively trivial given the symmetry of the detectors. Since the first two detectors are used by the FPGA to trigger a dust event, they collimate the particle beam so that the width and center is approximately the same as that of the pickup tube at the locations of the detectors. For trajectories that pass through all three collinear detectors, the corrections that correspond to a centered beam within each of the three pickup tubes represents the best estimate of the offsets of the DCS detectors. This is calculated using a numerical optimization

Plots Relative to Beamline at Third Detector (mm)

(a) Without offset corrections.

Plots Relative to Beamline at Third Detector (mm)
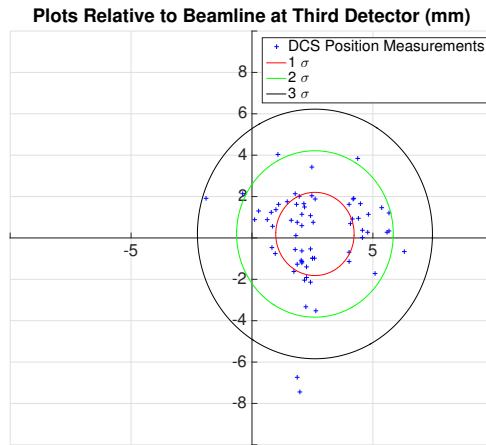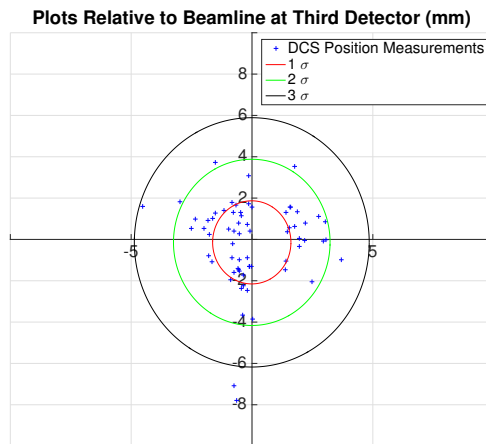
(b) With offset corrections.

Figure 3.2: Shown are 66 projected positions (looking down the beam towards the target chamber) at the location of the third pick-up tube detector. The 2D Gaussian is shown to indicate the approximate center of the dust particle beam. FIG 3.2a shows the projected beam profile before implementing the the DCS detector offset corrections. The beam is similarly off center for the other two pick-up tube detectors without offset corrections. Since the pick-up tubes function as beam collimators centered on beamline, the necessary corrections are numerically calculated in order to center the beam at the location of each pick-up tube as shown for the case of the third detector in FIG 3.2b.

routine which takes an ensemble of DCS 1 and 2 xy-position measurements and calculates the Gaussian center of the beam at the position of the three detectors. By stepwise adjustments, the routine provides the optimal corrections for both DCS 1 and 2 that place the Gaussian center so that it is aligned with the beamline for all three detector locations. Using a set of 66 trajectories, the offsets were computed as the following:

Mechanical Offset	DCS 1	DCS2
x	0.5 ± 0.2 mm	-2.1 ± 0.2 mm
y	0.3 ± 0.2 mm	-0.3 ± 0.2 mm

The mechanical uncertainty of ± 0.2 mm is due to the limited trajectory sample size. The xy-position measurements from DCS 1 and 2 are then adjusted using these fixed offsets when calculating three-dimensional trajectories.

The uncertainty of the x and y positions measured by DCS 1 and 2, after accounting for the offsets, is given by

$$\Delta x_{1,2} = \sqrt{(\Delta x_{electronic})^2 + (\Delta x_{mechanical})^2} \tag{3.8a}$$

$$\Delta y_{1,2} = \sqrt{(\Delta y_{electronic})^2 + (\Delta y_{mechanical})^2} \tag{3.8b}$$

where $\Delta x_{electronic}$ and $\Delta y_{electronic}$ are given by equations 3.7a and 3.7b respectively while $\Delta x_{mechanical}$ and $\Delta y_{mechanical}$ are the uncertainties in the xy-offset corrections.

Using both the DCS 1 and 2 uncertainties, the error in the projected particle position is given by the error propagation formula

$$\Delta x_{projected} = \sqrt{\left(\frac{\partial x_{projected}}{\partial x_1}\Delta x_1\right)^2 + \left(\frac{\partial x_{projected}}{\partial x_2}\Delta x_2\right)^2} \tag{3.9a}$$

$$\Delta y_{projected} = \sqrt{\left(\frac{\partial y_{projected}}{\partial y_1}\Delta y_1\right)^2 + \left(\frac{\partial y_{projected}}{\partial y_2}\Delta y_2\right)^2} \tag{3.9b}$$

where $\Delta x_{1,2}$ and $\Delta y_{1,2}$ are given by equations (3.8a) and (3.8b), $x_{1,2}$ and $y_{1,2}$ are the x and y positions measured by DCS 1 and 2 respectively, and $y_{projected}$ and $x_{projected}$ are given by equations

(2.4a) and (2.4b). Using equations (2.4a) and (2.4b), equations (3.9a) and (3.9b) can be written more explicitly as

$$\Delta x_{projected} = \sqrt{\left(\left(1 - \frac{z_{projected}}{d}\right)\Delta x_1\right)^2 + \left(\frac{z_{projected}}{d}\Delta x_2\right)^2} \tag{3.10a}$$

$$\Delta y_{projected} = \sqrt{\left(\left(1 - \frac{z_{projected}}{d}\right)\Delta y_1\right)^2 + \left(\frac{z_{projected}}{d}\Delta y_2\right)^2} \tag{3.10b}$$

where again $z_{projected}$ is the position anywhere along the beamline and d is the distance between DCS 1 and 2. Together, equations (3.10a) and (3.10b) can be used to construct two-dimensional error bars associated with projected xy-positions for any point along the beamline.

3.4   Summary

Together with the electronic error, determined using first principles and the look-up tables, and systematic error, determined using an estimation of mechanical offset, we can show two-dimensional error for transverse position anywhere along the beamline. In oder to verify the accuracy and precision of DCS, particle position measurements must be made independently and compared to predictions using DCS. This requires using a destructive position measurment method at a terminal point inside the target chamber. This, as well as a discussion on the instrument's sensitivity, is the topic of the next chapter.

Chapter 4

Instrument Performance

4.1   Introduction

DCS has been tested for sensitivity (e.g. minimum detectable charge), accuracy, and precision. Using the capability to match DCS and pick-up tube detector waveforms via timestamp matching, we can easily measure the trajectories for an ensemble of dust events and examine their corresponding velocity and charge data. From this we can empirically determine the sensitivity of DCS.

We also determine the accuracy and precision for trajectory measurements made by DCS by placing a target in the dust particle beam, observing the impact locations on the target, and comparing those locations with predicted locations based on DCS trajectories. The target chamber is an ideal location for this since it is where one is typically concerned with the characteristics of the beam allowing us to apply the determined accuracy and precision of DCS to future experiments. Since understanding the sensitivity of DCS is requisite to testing the trajectory accuracy, that is the first topic of this chapter.

4.2   Sensitivity

With a maximum acquisition rate of 40 million samples per second, the maximum particle velocity for which DCS can accurately measure position is limited. The zero intercept for equation (2.2) is approximately 8.1 km/s. This means that for particles with higher velocity, there are not enough data points for boxcar averaging to effectively smooth the signal without non-negligible

suppression of the transient peak. Detectability of low velocity particles is primarily determined by the length of transient data set by equations (2.1a) and (2.1b). This means that the time to upload transient data increases for lower velocities. A relevant concern may be the ability to acquire particle trajectories at a reasonable rate. This limitation is set by the data acquisition hardware, namely the GPIB upload speed.

The minimum charge of detectable particles is empirically determined to be approximately 6 fC and is set by the noise on the CSAs. The limitation on detectable charge relates to the range of detectable velocities for DCS, according to the natural bias of the overall accelerator dataset. Since the the fastest particles have the lowest charge [13], the upper velocity detection limit for DCS is also largely determined by the noise level. An overview of the range of detectable particle characteristics if shown in FIG 4.1.
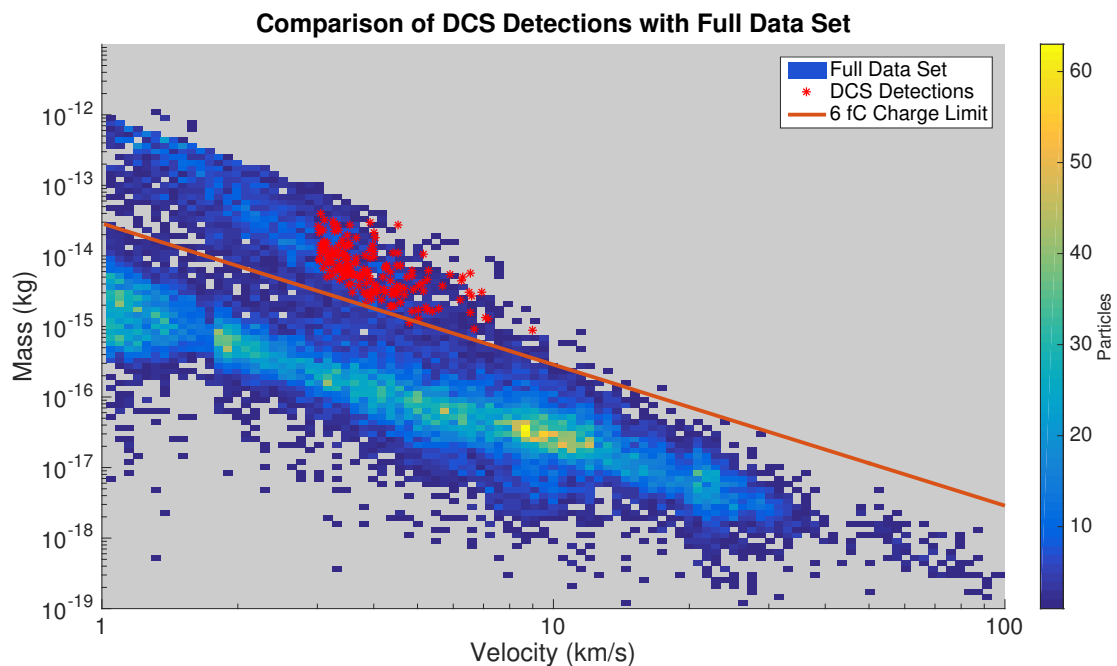
Figure 4.1: Experimental data from over 21,000 dust events (color plot) shown with 170 selected events detected by DCS (red). The 6 fC charge limit is shown and appears to be the approximate lower charge limit detectable by DCS. The apparent lower velocity limit at 3 km/s is an artifact of selected dust parameters for conducted experiments and does not represent a fundamental limitation for DCS. The upper velocity limit approaches 10 km/s and is limited by the data acquisition rate.

4.3   Trajectory Accuracy

In order to evaluate the accuracy of the trajectory measurements by DCS, we have performed a series of experiments in which we compare a set of projected impact points with an independent measurement of their locations. This has been done using a back lit 38.1 mm diameter aluminum-coated mirror. Since the coating is approximately 0.2 μm thick, some particle impacts locally remove the coating allowing light to pass through. With the mirror back lit, the impact points appear as small light spots, which are recorded with a digital camera.

The mirror is mounted inside of a 6 inch T-flange directly in front of a viewing window. Light is blocked both ways by wrapping the edge of the mirror mount in foil so that only light through holes in the coating is visible with the camera. An LED mounted within the assembly provides the interior light. The hardware for this apparatus was designed and built by a previous undergraduate student, Mikayla Roth. The mirror is mounted so that the beamline is orthogonal to its surface. A digital camera is placed just outside the viewing window facing the darkened side of the mirror. This is used to capture video footage of the appearance of light spots corresponding to particle impacts. The entire T-flange assembly is mounted on the back end of the target chamber, which is approximately 7.2 m from DCS 1 (see FIG 4.2).

Modifications to the target assembly were made so that images could have a visual reference to beamline. A marking system was designed and machined for this purpose. Using a high precision telescope aligned to the beamline, the marker is adjusted to coincide with the location of the beamline. The camera is then mounted with the marker temporarily obstructing the viewing window. The marker is captured by the camera footage so that all following light spots can be measured relative to beamline. After the marker is swept out of the field of view, the dust particle experiment commences.

The video captured by the camera is used to chronologically order and locate the appearance of each light spot. The light spots are located by their pixel indices in the image then transformed to physical coordinates relative to beamline. Image processing software was developed in Mathematica

to facilitate locating the pixels of individual light spots followed by a transformation to physical locations. This transformation is performed using a conversion based on a precise 1 cm scale line located on the impact surface of the mirror. The scale line was placed via titanium vapor deposition. Each appearance of a light spot in the camera footage is matched via timestamp to the corresponding dust event with a DCS trajectory measurement so that it can be compared to its predicted location.

4.3.1   Results

We used iron dust particles with radii in the range 1.1 - 2.6 μm, velocity in the range 1.1 - 2.5 km/s, and charge in the range 18 - 169 fC for the set of light spot location data. The relatively narrow velocity and size range is due to the requirement that the particles have sufficient kinetic energy to puncture the aluminum coating of the mirror. The range of available particles meeting this requirement was limited by accelerator performance. Iron was chosen since particles with lower density are less likely to puncture the aluminum coating making light spots difficult to find.

The accelerator was operated in "single shot mode" so that only one particle was allowed through at a time. This was done to avoid confusing multiple impacts on the mirror target permitting us to determine timestamp matching with high fidelity. An example of camera footage capturing light spots corresponding to dust particle impacts is shown in FIG 4.3.
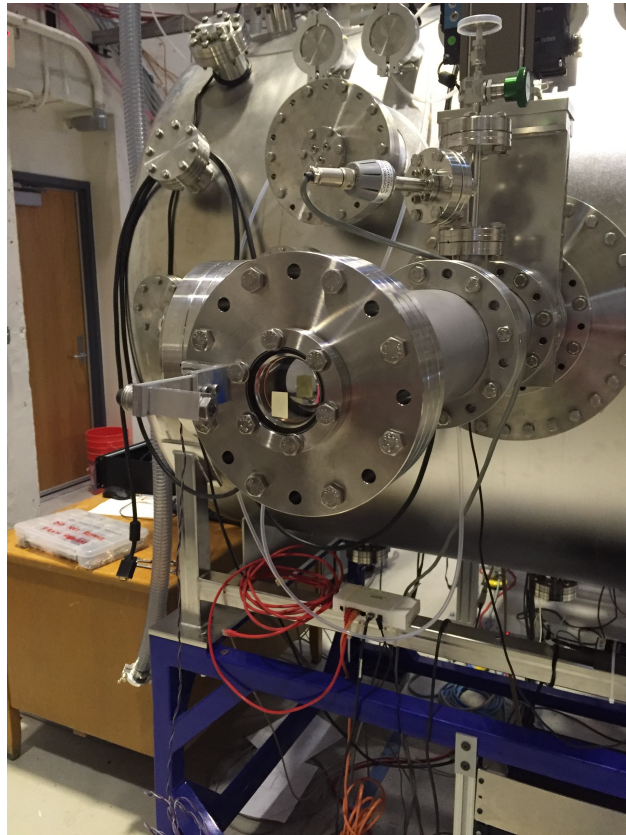
Figure 4.2: Mirror target assembly shown attached to the back of the target chamber. A digital camers is mounted so that it may capture footage of the appearance of light spots through the viewing window.
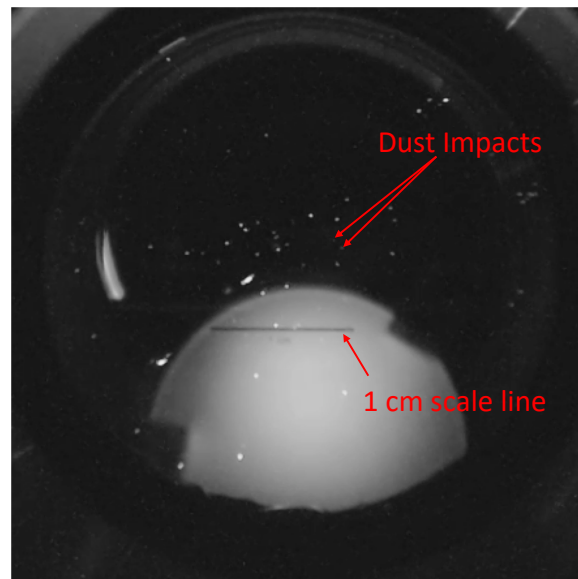
Figure 4.3: Camera footage of the mirror during an experiment. Two dust impact locations are shown with red arrows (very faint). Most of the points of light in this image are due to damage done during vapor deposition of the scale line. Impact locations are indicated by the appearance of a light spot occurring at a time matching the timestamp of a DCS trajectory measurement reaching the mirror.

Position Relative to Beamline at Back of Target Chamber (mm)
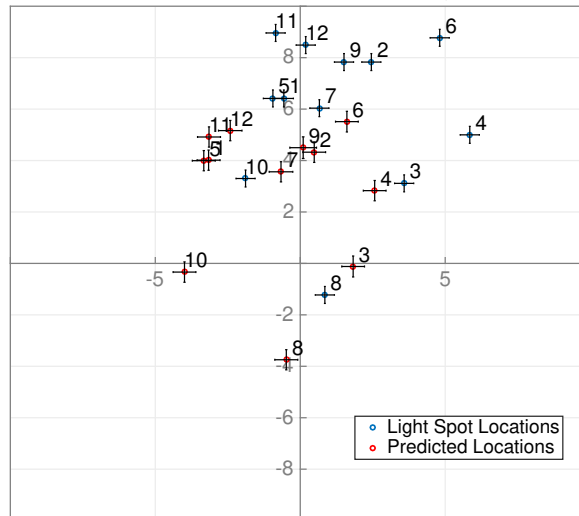
(a) Before correcting for systematic error.

Position Relative to Beamline at Back of Target Chamber (mm)
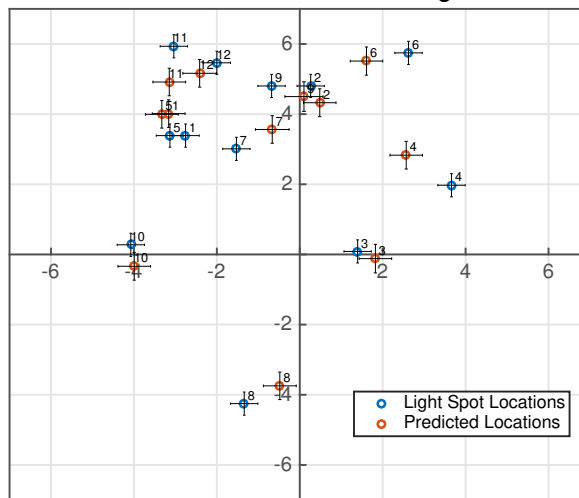
(b) After correcting for systematic error.

Figure 4.4: DCS predicted locations and Light Spot locations relative to beamline. FIG 4.4a shows how the grouping of light spot locations observed on the mirror target exhibit the same locations relative to each other as with the predicted locations only with a systematic error high and right. After adjusting for systematic error, the light spots can be seen with their time-corresponding predicted locations in FIG 4.4b. Clustering in the upper-left quadrant is a feature of the camera image making it easier to locate light spots in this area and is not due to DCS performance or beam characteristics.

The mirror and camera assembly contributed to systematic error in the light spot locations relative to beamline. This fact was made apparent by the light spot locations having the same grouping pattern as the predicted locations but with a clear shift shown in FIG 4.4a. This shift is quantified by the average difference between the light spot locations and predicted locations from DCS measurements in the data set. The light spot locations and DCS trajectory locations after correcting for systematic error are shown in FIG 4.4b.

The light spot locations have an associated xy-error of approximately 330 μm. Follow-up tests required a clean mirror without the scale bar marking. The camera and mirror configuration was left unaltered between tests. The uncertainty in pixel to physical length conversion was characterized by remounting the camera several times with a marked mirror and taking the average pixel length of the scale bar from single frame images. The resulting standard deviation was used as the error in light spot locations in subsequent data sets.

The discrepancy seen between the observed light spot locations and their predicted locations appears to worsen along the positive x-direction. The spatial dependence of this discrepancy was thought to be due to the geometrical relation between the camera, mirror target, and beamline. The mirror is mounted on an optical screw that allows it to pivot about the y-axis. Although the best attempt is made to place the mirror such that its surface is orthogonal to beamline, there is a slight deviation from this configuration (shown as θ in FIG 4.5).

From the geometry shown in FIG 4.5, we have the following trigonometric relationships,

$$\tan \theta = \frac{P}{x_T} \tag{4.1}$$

$$\tan \phi = \frac{x_A}{M} = \frac{x_T}{E} \tag{4.2}$$

where θ is the deviation of the mirror from the configuration where the beamline is orthogonal to its surface. ϕ is the incident angle of the apparent impact parameter, x_A, at the camera relative to beamline whereas x_T is the "true" impact parameter. P is the distance from the point of impact to the mirror/beamline intercept point along the beamline. M is the distance from the camera to the mirror/beamline intercept point along the beamline. E is the distance from the camera to the point

of impact along the beamline. From FIG 4.5, it can be shown that $E = M - P = M - x_T \tan \theta$. We can solve for x_T to get the following relation,

$$x_T = \frac{x_A}{1 + a x_A} \tag{4.3}$$

where a is the stretch parameter given as,

$$a = \frac{\tan \theta}{M} \tag{4.4}$$

We can characterize a spatially dependent discrepancy seen between an observed light spot location and its predicted location as the following,

$$\Delta x = |x_T(x_A) - x_A| \tag{4.5}$$

This expression is plotted in FIG 4.6. The number 4 light spot in FIG 4.4b, with an x-position at $\sim$4 mm, has a discrepancy in the x-direction with the corresponding predicted location of $\sim$2 mm. However, equation 4.5 does not predict this large of a discrepancy. Even for θ=15 deg, the contribution to discrepancy is on the order of a tenth of a mm. Therefore, the deviation of the mirror from an orthogonal configuration with the beamline does not significantly contribute to the discrepancies shown in FIG 4.4b. The apparent spatial dependence of location discrepancy may be due to an uncharacterized feature of the mirror/camera system or it may in fact be random.

4.4   Conclusion

The error on the predicted locations is computed using equations (3.10a) and (3.10b). The average computed error in this data set is the following: $\langle \Delta x_{projected} \rangle = 401 \mu$m and $\langle \Delta y_{projected} \rangle = 398 \mu$m. Measured error represents the average difference between predicted location and light spot locations after adjusting for systematic error in the light spot data. Overall, the measured xy-error for DCS trajectory plots at this location on the beamline is approximately $\pm$ 530 μm and appears to be random. The method for calculating error described in chapter 3 is supported by the results of this experiment. Where particle position was only known to within roughly 1 cm^2 prior to the the use of DCS, it can now be known to within 1 mm^2 at the back of the target chamber.
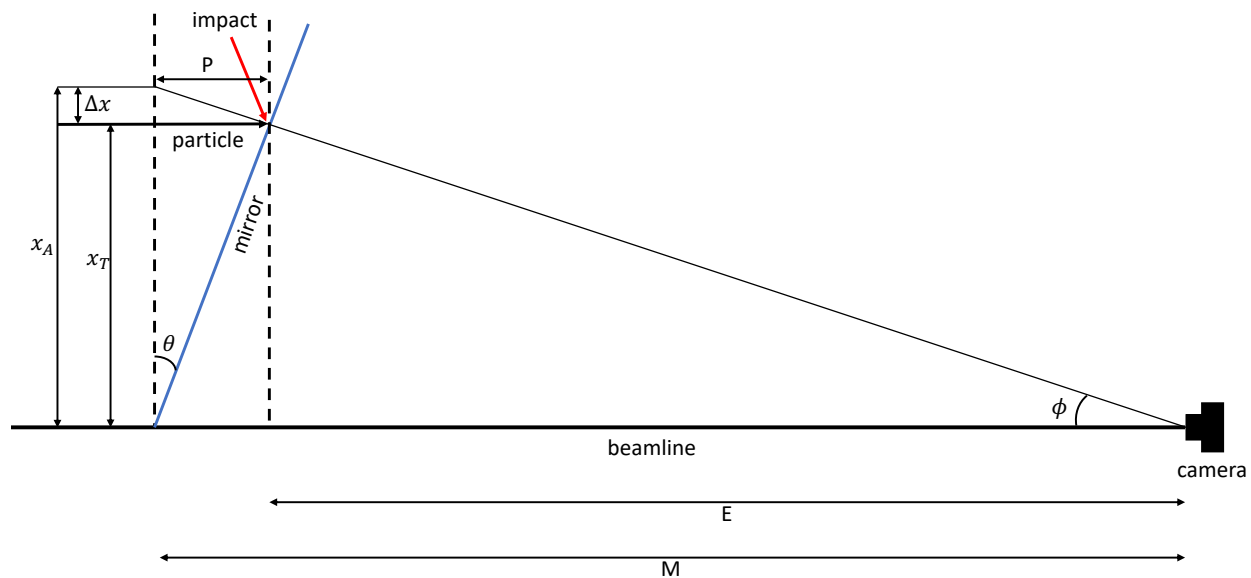
Figure 4.5: Illustration of the geometric relation between the camera, mirror target, and beamline (looking down along the y-axis, not to scale). The mirror target deviates by an angle θ from the configuration where its surface would be orthogonal to beamline. A particle impacts the surface of the mirror with a "true" impact parameter, x_T. The image of this impact is observed by the camera at an angle ϕ and at position x_A relative to beamline. Δx is the discrepancy between x_T and x_A. M is the the distance from the camera to the point where the mirror surface intercepts the beamline. P is the distance from the observed impact location to the actual point of impact on the mirror along the beamline. E is the distance from the camera to the point of impact along the beamline.

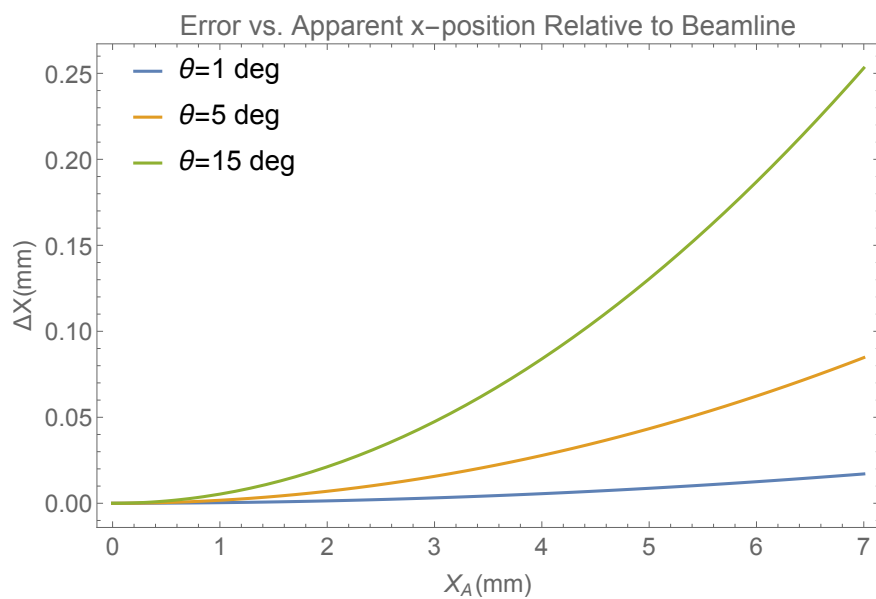Figure 4.6: Equation (4.5) is plotted using three separate values of θ in the stretch parameter, a, given by equation (4.4). The value of M was measured as ~ 5 cm and is used in this calculation.

Chapter 5

Conclusion

Characterizing the dust beam on the University of Colorado Dust Accelerator, such as adjusting the fine scale aiming or focusing, has been difficult in the past without immediate feedback. This has previously required placing a target in the beamline and recording thousands of impact points in order to obtain an aggregate image of the beam spot [13]. Given the level of performance by DCS, we are able to actively measure beam characteristics in real time with the additional capability of measuring spot size at any point along the beamline based on three-dimensional trajectories.

With improvements to DCS precision, we would like to use trajectory measurements to locate individual impact craters. The relation between impact crater and impactor characteristics will be analyzed and compared to previous studies. Without the ability to trace individual particles to their point of impact, studies had to be performed using large ensembles of impacts [8]. Crater models based on scaling laws were then tested by comparing averages from data sets containing both particle and crater characteristics [19]. DCS trajectory measurements used to locate impact craters will build upon experimental testing of previously used crater scaling models by providing one-to-one correspondence between individual impact craters and their impactors [19, 8, 20, 21].

A 1 mm^2 search area is still too large to be able to practically locate 1 μm diameter craters under a scanning electron microscope (SEM). One way to reduce the size of the search area (i.e. the projected position uncertainty) may be to reduce the noise level on the wire electrode channels. Another method may be to increase the number of wire electrodes in each detector. However, with each wire being 0.48 mm thick, this would begin to partially block the particle beam where part of

the original purpose is to measure position with minimal disturbance. Nevertheless, locating and analyzing individual impact craters is one the the main scientific goals of DCS.

The dual detector DCS has been successfully integrated with the Colorado dust accelerator. New data acquisition and signal processing software enables the dual configuration of DCS to provide previously unknown dust particle trajectories. These trajectories have been verified using an independent measurement of impact locations. With reliable false signal rejection, DCS can operate continuously during any experiment. Precise trajectory measurement along the beamline enables new options for instrument calibration, scientific experiments, and improvement of the accelerator performance.

Bibliography

[1] ESO/Y. Beletsky. Zodiacal light over la silla, November 2014.

[2] Eberhard Grün, Bo Gustafson, Stan Dermott, and Hugo Fechtig. Interplanetary Dust. Springer, 2001.

[3] J. F. Friichtenicht and J.C. Slattery. Ionization associated with hypervelocity impact. Technical report, NASA, 1963.

[4] B.-K. Dalmann, E. Grün, J. Kissel, and H. Dietzel. The ion-composition of the plasma produced by impacts of fast dust particles. Planetary and Space Science, 25(2):135 – 147, 1977.

[5] H Dietzel, G Eichhorn, H Fechtig, E Grun, H J Hoffmann, and J Kissel. The heos 2 and helios micrometeoroid experiments. Journal of Physics E: Scientific Instruments, 6(3):209, 1973.

[6] M. Horanyi, Z. Sternovsky, M. Lankton, C. Dumont, S. Gagnard, D. Gathright, E. Grün, D. Hansen, D. James, S. Kempf, B. Lamprecht, R. Srama, J. R. Szalay, and G. Wright. The lunar dust experiment (LDEX) onboard the lunar atmosphere and dust environment explorer (LADEE) mission. Space Sci. Rev., 185(1-4):93–113, December 2014.

[7] R. Srama, T. J. Ahrens, N. Altobelli, S. Auer, J. G. Bradley, M. Burton, V. V. Dikarev, T. Economou, H. Fechtig, M. Gorlich, M. Grande, A. Graps, E. Grun, O. Havnes, S. Helfert, M. Horanyi, E. Igenbergs, E. K. Jessberger, T. V. Johnson, S. Kempf, A. V. Krivov, H. Kruger, A. Mocker-Ahlreep, G. Moragas-Klostermeyer, P. Lamy, M. Landgraf, D. Linkert, G. Linkert, F. Lura, J. A. M. McDonnell, D. Mohlmann, G. E. Morfill, M. Muller, M. Roy, G. Schafer, G. Schlotzhauer, G. H. Schwehm, F. Spahn, M. Stubig, J. Svestka, V. Tschernjawski, A. J. Tuzzolino, R. Wasch, and H. A. Zook. The cassini cosmic dust analyzer. Space Sci. Rev., 114(1-4):465–518, 2004.

[8] Anthony Shu, Sebastian Bugiel, Eberhard Grün, Jon Hillier, Mihály Horányi, Tobin Munsat, and Ralf Srama. Cratering studies in polyvinylidene fluoride (PVDF) thin films. Planetary and Space Science, 89:29 – 35, 2013.

[9] M. Horanyi, V. Hoxie, D. James, A. Poppe, C. Bryant, B. Grogan, B. Lamprecht, J. Mack, F. Bagenal, S. Batiste, N. Bunch, T. Chanthawanich, F. Christensen, M. Colgan, T. Dunn, G. Drake, A. Fernandez, T. Finley, G. Holland, A. Jenkins, C. Krauss, E. Krauss, O. Krauss, M. Lankton, C. Mitchell, M. Neeland, T. Reese, K. Rash, G. Tate, C. Vaudrin, and J. Westfall. The student dust counter on the new horizons mission. Space Sci. Rev., 140(1-4):387–402, October 2008.

[10] T. See, M. Albrooks, D. Atkinson, and C. Simon. Meteoroid and debris impact features documented on the long duration exposure facility. Technical report, National Aeronautics and Space Administration Houston TX Lyndon B Johnson Space Center, 1990.

[11] A. Auer and K. Sitte. Detection technique for micrometeoroids using impact ionization. Earth and Planetary Science Letters, 4(2):178 – 183, 1968.

[12] D. O. Hansen. Mass analysis of ions produced by hypervelocity impact. Applied Physics Letters, 13(3):89–91, 1968.

[13] Anthony Shu, Andrew Collette, Keith Drake, Eberhard Grün, Mihály Horányi, Sascha Kempf, Anna Mocker, Tobin Munsat, Paige Northway, Ralf Srama, Zoltán Sternovsky, and Evan Thomas. 3 mv hypervelocity dust accelerator at the colorado center for lunar dust and atmospheric studies. Rev Sci Instrum, 83(7):075108, Jul 2012.

[14] National Electrostatics Corp.kernel description. `http://www.pelletron.com/necloc.htm`. Accessed: 2017-08-25.

[15] Siegfried Auer. Two high resolution velocity vector analyzers for cosmic dust particles. Review of Scientific Instruments, 46(2):127–135, 1975.

[16] Katharina A. Otto, Ralf Srama, Siegfried Auer, Sebastian Bugiel, Eberhard Grün, Sascha Kempf, and Jianfeng Xie. Application and calibration of a simple position detector for a dust accelerator. Nuclear Instruments and Methods in Physics Research Section A: Accelerators, Spectrometers, Detectors and Associated Equipment, 729:841 – 848, 2013.

[17] Paige Northway, Siegfried Auer, Keith Drake, Mihaly Horanyi, Anna Mocker, Tobin Munsat, Anthony Shu, Zoltan Sternovsky, Evan Thomas, and Jianfeng Xie. Characteristics of a new dust coordinate sensor. Meas. Sci. Technol., 23(10), October 2012.

[18] Siegfried Auer, Eberhard Grün, Sascha Kempf, Ralf Srama, André Srowig, Zoltan Sternovsky, and Valentin Tschernjawski. Characteristics of a dust trajectory sensor. Rev Sci Instrum, 79(8):084501, Aug 2008.

[19] A. J. Shu. Microcratering in Polyvinylidene Fluoride. PhD thesis, University of Colorado at Boulder, 2015.

[20] Andrew Poppe, Brian Jacobsmeyer, David James, and Mihály Horányi. Simulation of polyvinylidene fluoride detector response to hypervelocity particle impact. Nuclear Instruments and Methods in Physics Research Section A: Accelerators, Spectrometers, Detectors and Associated Equipment, 622(3):583 – 587, 2010.

[21] M. Lambert. Hypervelocity impacts and damage laws. Advances in Space Research, 19(2):369 – 378, 1997. Space Debris.